Design and Fabrication of Antennas Using 3D Printing

Jason Bjorgaard[1], Michael Hoyack[2], Eric Huber[3], Milad Mirzaee[4],
Yi-Hsiang Chang[5], and Sima Noghanian[4, *]

Abstract—Due to a recent growth in three-dimension (3D) printing technology, engineers can fabricate affordable and versatile antennas; however, lossy conductive materials, inadequate antenna terminations, and simplistic designs which do not adequately utilize the available volume continue to limit the capabilities of 3D printed antennas. In this work, the dielectric constants of three polylactic acid (PLA) materials, dielectric PLA, magnetic PLA and conductive PLA, were measured using the coaxial transmission line method, and the results were compared with measurements using the commercially available coaxial probe method. Based on published dielectric constants for solid non-printed PLA, a variety of antenna designs were simulated and fabricated. Each of these antenna designs addressed a certain shortcoming faced by 3D printed antennas. The antennas were designed with a target resonant frequency of 2.45 GHz, an impedance bandwidth of at least 500 MHz, and a gain greater than 1.5 dBi. The three antennas presented here are a fractal bow-tie antenna (FBTA), a spiral antenna, and a Yagi-Uda antenna.

1. INTRODUCTION

Recently, 3D printing technology has been increasingly used for the fabrication of 3D electromagnetic structures. This method has several advantages over traditional fabrication methods including a smaller form-factor, lighter weight, lower cost and being more bio-friendly. Over the past few years, 3D printing has been utilized for the fabrication of antennas [1–10]. In [1–4] 3D printing was used for the fabrication of the substrate part of the antenna. In these designs, the prototype of the antenna was fabricated using available 3D printing substrate materials, and then the radiator part was created by coating a conductive material on the 3D printed layers. In [5, 6] the dielectric and conductive parts of the antenna were both fabricated using 3D printing and as an integrated process. Novel 3D printing methods using direct writing of a silver nanoparticle ink [7] on the internal surfaces of glass hemisphere were investigated in [8], which makes the integration of an antenna directly onto the package of a small wireless sensor node possible. Direct printing of the conductive traces on the 3D printed substrates was studied in [9]. 3D printing has facilitated the fabrication of the lens antennas for the millimeter wave frequencies with comparable performance to those built with conventional methods [10–12].

This paper focuses on the various aspects of using additive manufacturing for antenna fabrication. For this goal it is necessary to first characterize the dielectric properties of the 3D printing materials such as polylactic acid (PLA) materials. The next step is to examine the suitability of various antenna designs, and finally, designing the connector for antenna's termination. For the antenna designs, we used PLA, a high-strength thermoplastic material [13]. For material characterization, the dielectric constant of the PLA was determined by finding the complex permittivity. The real component of permittivity is the ability of a material to store electric energy, whereas the imaginary component is the loss factor of the material [14].

Along with the development of 3D printing technology for the fabrication of antennas, determining a method to attach a connector to the antennas is getting important. The conductive materials were found not to adhere well enough to the PLA to adequately support the sub miniature version A (SMA) connector [15]. This led to unnecessary radiation performance losses. We investigated some methods to avoid the direct attachment of an SMA connector to the 3D printed antenna terminal. In this work, three different antenna designs were considered. The first design is based on a Sierpinski fractal shape. Due to the complex geometry of fractal designs, these antennas are capable of resonating at multiple frequencies [16], making them excellent wideband antennas. The second design is a spiral antenna. Spiral antennas are circularly polarized wideband antennas [17] with geometries determined by the wavelength of the desired operation frequencies [18]. The final design is a Yagi-Uda antenna comprised of a half-wavelength dipole and a parasitic element to improve the radiation properties of the antenna [15].

2. MATERIAL CHARACTERIZATION

2.1. Test Method Selection

The first step was to characterize the dielectric properties of the chosen 3D printing materials. There are many available test methods that can be utilized to accomplish this, each with advantages based on the available equipment, material sample shapes, material properties, and a multitude of other factors [14]. Among them, the transmission line method was chosen. The advantages of the transmission line method are that it is "broadband, which is the best method for lossy to low loss materials, it can be performed on machinable solids" [14] and it does not require precision machining. The results from this method were compared to those measured using a Keysight 85070E dielectric probe to validate the accuracy of the method.

2.2. Test Apparatus

When measuring unknown material characteristics, the dielectric constant may change dramatically as a function of frequency. The test apparatus chosen to measure the material properties was a coaxial transmission line, shown in Figure 1, which was designed for use at the frequency range of 1.7 GHz to 4 GHz. The power source generates an electromagnetic (EM) wave that travels through the transmission line. Using a slotted line, the EM wave was then used to compute the voltage standing wave ratio (VSWR) and phase shift when a material sample was placed in the material chamber. With these measurements, the permittivity and loss tangent values of the dielectric material were calculated from the reflection coefficient and the impedance of the transmission line.

Figure 1. Coaxial cable slotted line.

The coaxial transmission line consisted of a slotted line and a chamber for the sample material. The coaxial transmission line was made from brass tubing for the outer conductor and a brass rod for the inner conductor. The brass tubing was divided into the two sections of the coaxial transmission line, each 14 inches in length. This allowed for two 1.7 GHz wavelengths to be present within the material chamber. The outer conductor of the coaxial transmission line was made with connectors between the slotted line and material chamber to allow for the coaxial transmission line to be disassembled. At each end of the coaxial transmission line, Amphenol's RF Bayonet Neill-Concelman (BNC) connectors were soldered to connector caps. These caps formed connection joints to the outer conductor, while the inner

conductor of the BNC formed a clean connection joint to the inner conductor of the transmission line. The caps are removable to allow for the PLA materials to be inserted into the coaxial transmission line.

Using a lathe, the inner conductor was machined to a diameter to match the impedance of a $50\,\Omega$ coaxial line. The characteristic impedance was found through Equation (1) where η_o is the impedance of free space, ε_r is the relative permittivity, μ_r is the relative permeability of the material, D_o is the diameter of the outer conductor, and d_i is the diameter of the inner conductor.

$$Z_o = \sqrt{\frac{L}{C}} = \frac{\eta_o}{2\pi\sqrt{\varepsilon_r\mu_r}} \ln\left(\frac{D_o}{d_i}\right) \tag{1}$$

Because the outer conductor had a diameter of 0.817 inches (2.075 cm), the diameter of the inner conductor was determined to be 0.355 inches (0.902 cm). Ultra-high-molecular-weight (UHMW) polyethylene was used to suspend the inner conductor in the transmission line, therefore, the diameter of this section of the inner conductor was turned to account for the permittivity of the UHMW Polyethylene. Using Eq. (1) with $\varepsilon_r = 1.907$ for UHMW Polyethylene and $D_o = 0.817$ inches (2.075 cm), the resultant diameter for the inner conductor was 0.229 inches (0.582 cm) to achieve an impedance of $50\,\Omega$. A hole was drilled at the end of the inner conductor to allow placement of a female jack. The BNC inner conductor is able to be mated with the female jack to ensure a clean connection. Figure 2 shows the inner conductor of the transmission line (a) and the inner conductor being supported by the UHMW Polyethylene (b).

(a)   (b)

Figure 2. (a) Inner conductor of the coaxial transmission line, (b) inner conductor supported by the UHMW in the transmission line.

After the load impedance and reflection coefficient were calculated for free space, sample blocks of PLA were placed within the coaxial line. The presence of a material sample in the coaxial line results in a shift in matching. By calculating the load impedance from the slotted line for each material, the permittivity and loss tangent can be found by calculating the shift in reflection coefficient. Eq. (1) shows the impedance of the line in terms of line dimensions and material. Using Eqs. (2)–(5), the resistance (R), inductance (L), capacitance (C), and conductance of the coaxial transmission line (G) were determined, respectively, where R_s is the resistivity of the conductor, ε' is the real component of permittivity, ε'' is the imaginary component of permittivity.

$$R = \frac{R_s}{2\pi}\left(\frac{1}{D_o} + \frac{1}{d_i}\right) \tag{2}$$

$$L = \frac{\mu}{2\pi}\ln\left(\frac{D_o}{d_i}\right) \tag{3}$$

$$C = \frac{2\pi\varepsilon'}{\ln\left(\dfrac{D_o}{d_i}\right)} \tag{4}$$

$$G = \frac{2\pi\varepsilon''}{\ln\left(\dfrac{D_o}{d_i}\right)} \tag{5}$$

Based on the results of Eqs. (2)–(5), Eq. (6) was used to calculate the shifted reflection coefficient (Γ_{shifted}) in the transmission line. By finding the shift in reflection coefficient in the transmission

line, the loss tangent ($\tan\delta$) was calculated using Eq. (7) by dividing the imaginary component of the permittivity with the real component of the permittivity. Eqs. (1)–(7) can be found in [19];

$$\Gamma_{\text{shifted}} = \Gamma e^{-j2\sqrt{(R+j\omega L)(G+j\omega C)}l} \tag{6}$$

$$Z = \frac{\Gamma_{\text{shifted}} + 1}{1 - \Gamma_{\text{shifted}}}$$

$$\tan\delta = \frac{\varepsilon''}{\varepsilon'} \tag{7}$$

2.3. Measurement Results

Table 1 shows the calculated dielectric constant and loss tangent values for the coaxial transmission line method at 1.7 GHz to 4 GHz.

Table 1. Average values for dielectric constant and loss tangent at 1.7 GHz–4 GHz.

Material	Dielectric Constant	Loss Tangent
Dielectric PLA	2.533	0.0395
Conductive PLA	9.349	0.0020

To verify the results from coaxial transmission line method, a Keysight dielectric probe 85070E was used to measure the dielectric constant and loss tangent at a frequency range of 1 GHz to 10 GHz [20]. It was found that for the conductive PLA the dielectric constant decreases from 9.3 at 1 GHz to 6.6 at 10 GHz. The loss tangent values for conductive PLA vary widely as a direct function of frequency. The values from the dielectric probe measurements at 2.4 GHz are shown in Table 2. Please note that the loss tangent for dielectric PLA was too low to be measured.

Table 2. Values for dielectric constant and loss tangent from dielectric probe measurement at 2.4 GHz.

Material	Dielectric Constant	Loss Tangent
Dielectric PLA	2.473	-
Conductive PLA	9.001	0.080

Comparing the coaxial transmission line method to the probe method at the frequency range for the antenna design, the difference was only 2.55%. For the conductive PLA, the difference between the probe and coaxial transmission methods was 3.87%. In conclusion, the dielectric constants for coaxial transmission line method and dielectric probe method are within 5% accuracy of each other.

3. ANTENNA DESIGN

Three unique designs, a fractal bow-tie antenna, a spiral antenna, and a Yagi-Uda antenna, were chosen and simulated using ANSYS HFSS [21] and CST Microwave Studio [22].

3.1. Fractal Bowtie Antenna

For the embedded bow-tie design, a Sierpinski fractal was applied to a bow-tie antenna. The fractal bow-tie antenna (FBTA) had a desired resonant frequency f of 2.5 GHz; therefore, a wavelength λ of 125 mm in free-space was calculated. The length of the FBTA was designed to be approximately 60 mm. The goal of this design was to build an antenna with a gain greater than 1.5 dBi and a -10 dB reflection coefficient bandwidth of greater than 500 MHz. Multiple variations of the radiator design were simulated, with the best performing geometry having a 1st iteration fractal and a step in the radiator thickness, being twice the thickness near the center. Values for dielectric PLA permittivity and

loss tangent were 3.1 and 0.1, respectively, originally determined from [23]. The coaxial cable method provided values of permittivity of 2.533 and loss tangent of 0.0395.

FBTA Rev 1 is the antenna designed based on the values provided in [23]. The key dimensions for FBTA Rev 1 are shown in Figures 3(a) and (b). FBTA Rev 2 was designed based on the accurate slotted line measurements by adding 1 mm in the 39.2 mm overall length of the radiators to bring the resonant frequency back down to 2.5 GHz, as shown in Figure 3(c). The reflection coefficients of both Rev 1 and Rev 2 with different permittivity values are shown in Figure 4.
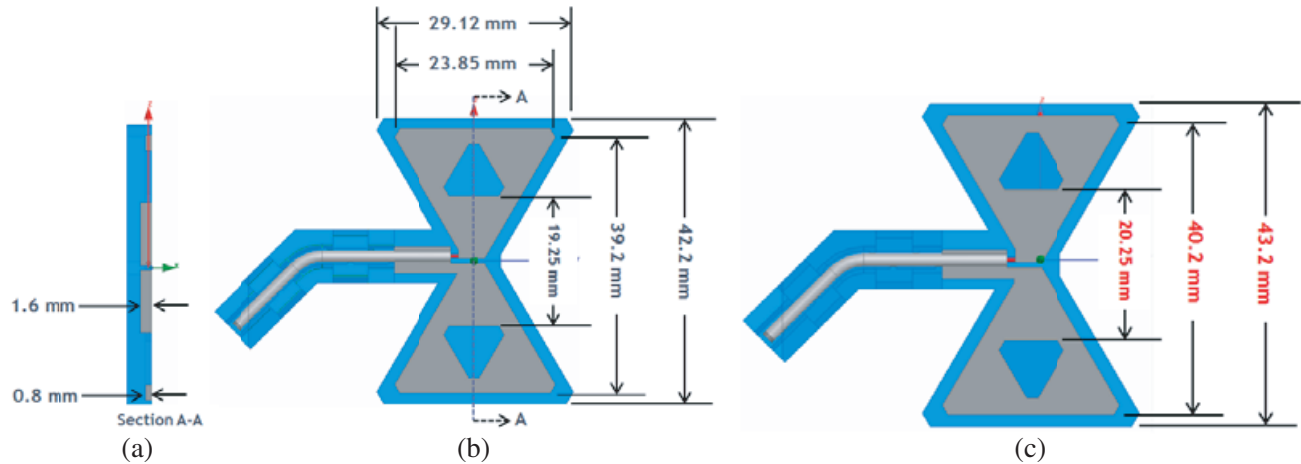
Figure 3. FBTA (a)–(b) Rev 1 key dimensions, (c) revised dimensions for Rev 2.
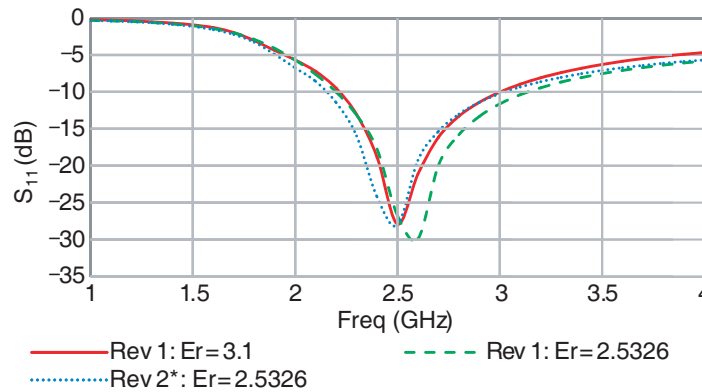
Figure 4. Reflection coefficients for FTBA antennas.

3.2. Spiral Antenna

The second antenna design was an Archimedean spiral antenna. Spiral antennas are frequency independent antennas that have resonating frequencies based on the geometry of the antenna. These antennas are typically wideband antennas that are easy to fabricate, relatively inexpensive, and highly efficient. For 3D printing, this design is very beneficial because it could either be constructed using the conductive PLA, printed using PLA and painted with a conductive material, or embedded into a PLA substrate using conductive materials post printing. In order to achieve the desired behavior, the inner radius was set equal to the arm width. Through optimization, it was determined that the optimum inner radius and arm width was 2.55 mm with a spacing of 1.91 mm. The arm width was 2.55 mm and the outer radius was 1.675 mm. The resultant antenna is shown in Figure 5. Simulation results showed the spiral has a gain of 3.31 dBi at 2.45 GHz. with a wide bandwidth of 2.3 GHz–11.4 GHz.
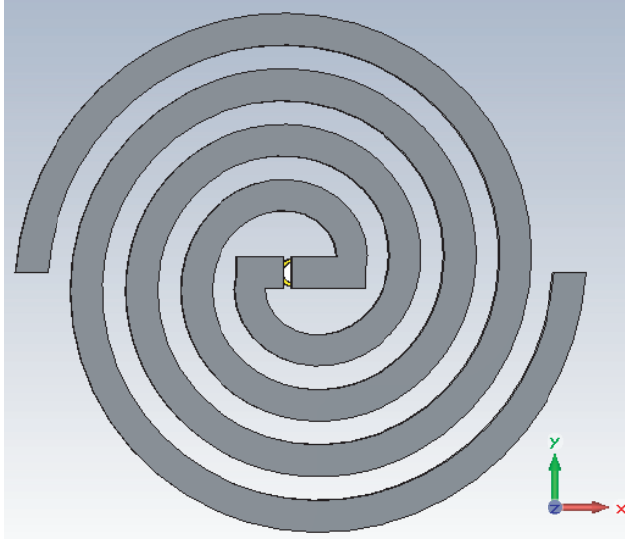
Figure 5. Spiral design, 1: inner radius, 2: arm width, 3: outer radius.
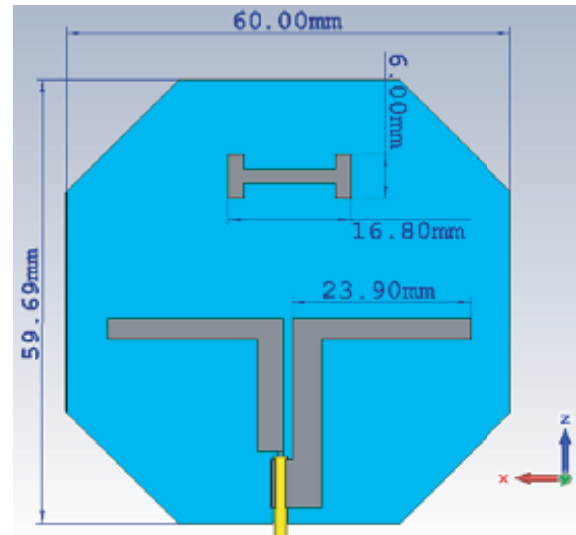
Figure 6. Yagi-Uda antenna design.

3.3. Yagi-Uda Antenna

This design is a simple half-wavelength dipole with a rectangular parasitic element on a square substrate as shown in Figure 6. The a barbell shape parasitic element improved the simulated gain from 2.43 dBi (straight parasitic element) to 2.58 dBi, at 2.45 GHz. The −10 dB bandwidth was from 2.1 GHz to 2.8 GHz with a directional radiation pattern.

4. CABLE CONNECTION DESIGN

4.1. Fractal Bow-Tie and Yagi-Uda Antennas Termination Design

In [15] the challenge of attaching an SMA connector to the Yagi-Uda antenna was discussed. To overcome these challenges, a direct cable launch was proposed to connect the FBTA and Yagi-Uda antennas to a 50 Ω RG-405 conformable coaxial cable. For reference, the original Yagi geometry was simulated in ANSYS HFSS with an edge launch SMA, as shown in Figure 7(a). In the proposed new method, the distance from the cable outer conductor to the radiator gap, shown in Figure 7(b), was optimized for both the SMA and direct cable fed Yagi-Uda antennas. The bent cable channel provides both axial and rotational retentions for the cable, preventing the cable to conductive paint joint from being compromised. This is an improvement over the SMA jack edge launch connector, which had no practical means of strain relief or mechanical mounting to the antenna substrate, allowing the connector to move or fall off when handling or mating an SMA cable plug. The reflection coefficient of the optimized antennas are shown in Figure 8. Per Figure 8 and Table 3, the direct cable fed Yagi-Uda simulated gain improved from 1.25 dBi to 1.49 dBi, recognizing the direct cable feed as a potential improvement both mechanically and electrically.

The same study comparing an SMA launch was performed in HFSS for FTBA. This required altering the FBTA design to be fed with an edge launch SMA, as shown in Figure 9(a). Table 4

Table 3. Gain and bandwidth of SMA and direct cable fed Yagi-Uda antenna.

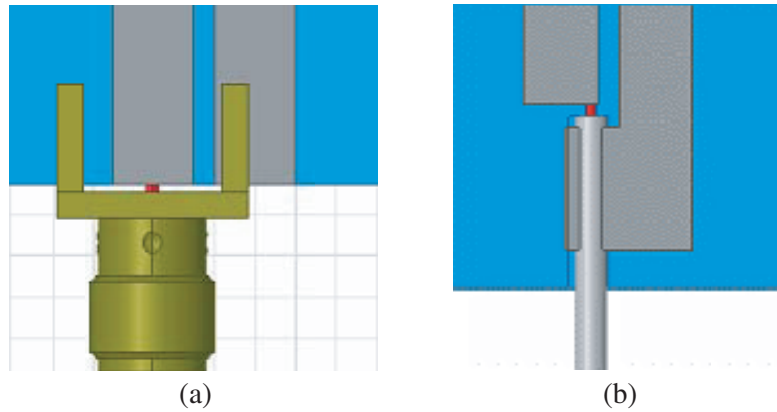| Design	Gain (dBi)	−10 dB Bandwidth (GHz)
Direct Cable Fed Yagi-Uda	2.75	0.75
SMA Fed Yagi-Uda	1.49	0.75

(a)   (b)

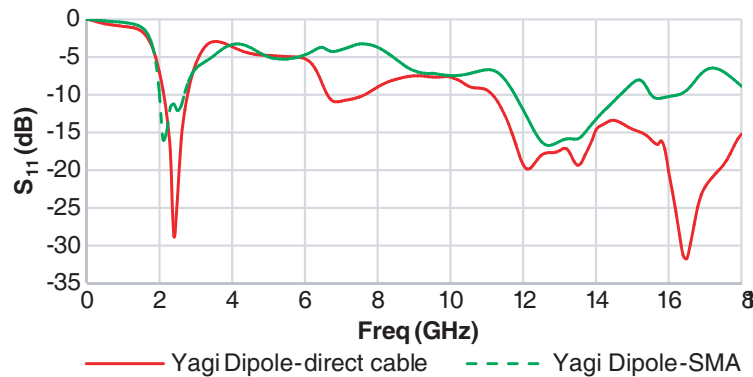**Figure 7.** Yagi-Uda antenna launch gap of (a) SMA feed, (b) direct cable feed.

Figure 8. Reflection coefficient for of SMA (blue) and direct cable (red) fed Yagi-Uda antenna.

**Table 4.** Gain and bandwidth of SMA and direct cable fed FTBA antenna.

Design	Gain (dBi)	-10 dB Bandwidth (GHz)
Direct Cable FBTA	1.99	0.80 GHz
SMA fed FBTA	1.84	0.38 GHz

summarizes the gain and bandwidth comparisons. Figure 10 shows the reflection coefficient. These results show that the direct cable fed FBTA was an improvement in both gain and bandwidth over the SMA fed FBTA.

Considering 3D printed resolution limitations, the cable retention was designed using a single bend in the cable channel. Grooves were added in two places along the channel for placing zip tie cables to hold the cable in channel. The bent cable channel provides both axial and rotational retention for the cable, preventing the cable to conductive paint joint from being compromised. This overall design is shown in Figure 11.

## 4.2. Spiral Antenna Termination Design

Due to the nature of the spiral antenna radiators, which required a mechanical support, and the sensitivity of the radiator spacing, a separate, non-conductive PLA fixture was developed, shown as the purple geometry in Figure 12. Numerous design changes occurred to achieve optimal S_{11} performance in simulation, leading to a separate PLA fixture with standoffs to hold the radiators in position while maintaining a small footprint to minimize the near field interaction with the radiators. A hole was

(a) (b)
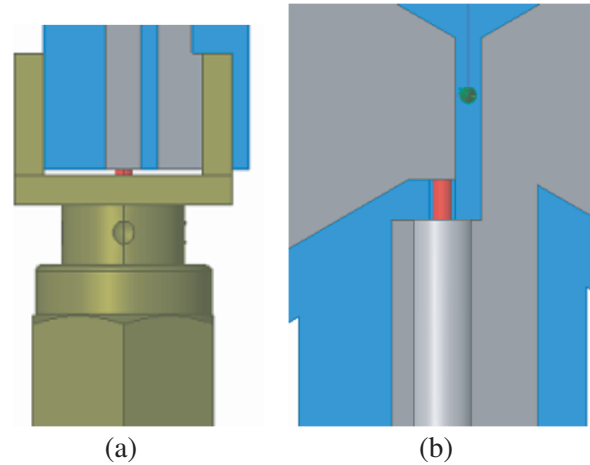
**Figure 9.** FBTA launch gap of (a) SMA feed, (b) direct cable feed.
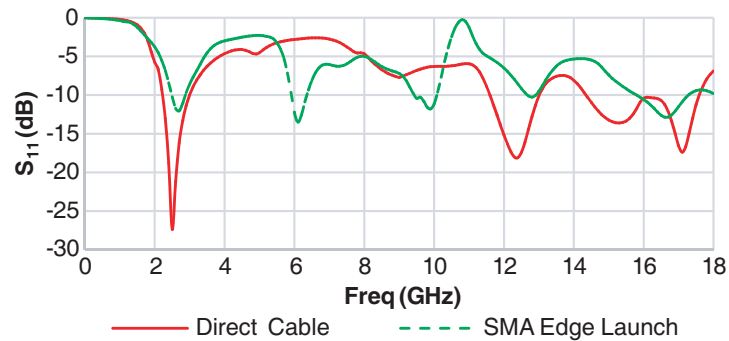
Figure 10. Reflection coefficient of SMA (blue) and direct cable (red) fed FBTA.

(a) (b)
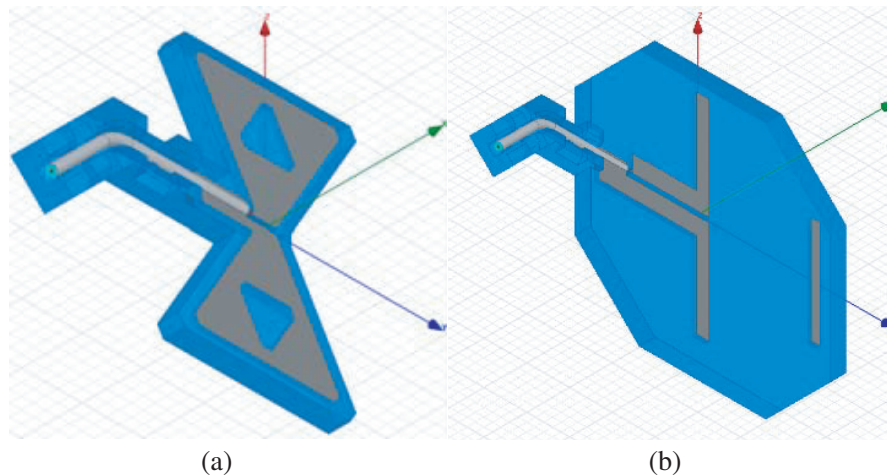
Figure 11. Overall cable retention geometry on (a) FBTA, and (b) Yagi-Uda.

designed in the middle of the PLA fixture for inserting the cable until the cable dielectric is flush with the radiator mounted surface. On the top of each PLA fixture standoff is a square hole for accepting small cylindrical locating pins found on the bottom surface of the radiators. The radiators are assembled onto the PLA fixture, with a slight interference fit between the radiator pins. One radiator has a small
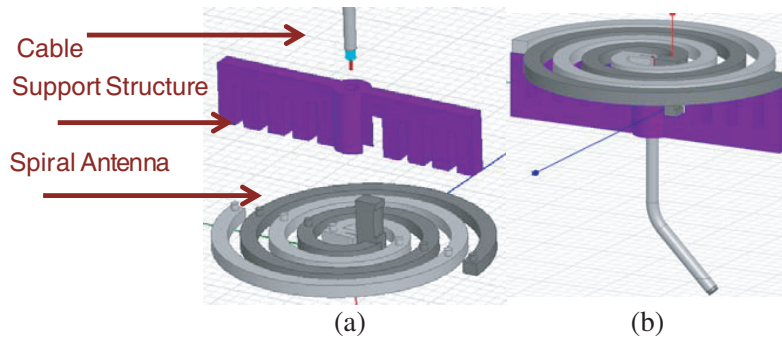
**Figure 12.** Spiral antenna cable termination (a) exploded view, and (b) assembled.

slot in the end to accept the center conductor of the cable, while the other has a protrusion that touches the outer coductor of the cable. A zip tie is secured around the PLA fixture and ground radiator protrusion to maintain a good contact joint between the cable outer conductor and radiator.

5. ANTENNA FABRICATION

Once simulations were complete, the geometry of the antenna designs were built using Printrbot Play 3D printer (FBTA) and Robo R1 + 3 3D printer (Yagi-Uda and Spiral). These printers were used due to their availability to the authors. Depending on the design, different post-printing fabrication steps were required to construct the antennas.

5.1. Fractal Bowtie Antenna

Several samples of the FBTA Rev 1 were fabricated using three different conductive materials to fill the radiator cavities in the PLA housing, as shown in Figure 13. The conductive materials were dispersed carbon pigment paint manufactured by Bare Conducive® [24], copper paint manufactured by Caswell Inc. [25], and 99.99% pure Gallium [26].
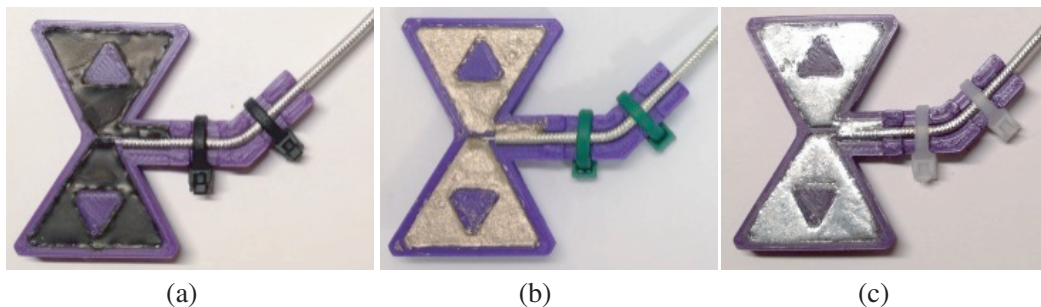

Figure 13. Assembled FBTA Rev 1 with (a) carbon conductive paint, (b) copper conductive paint, and (c) gallium radiators.

The conductive paints were applied by carefully dripping small quantities into the radiator cavities manually, until the paint was flushed with the top of the PLA housing. For the gallium, the 29.77°C melting point allowed it to be poured into the radiator cavities, but due to the surface tension of the melted gallium, a secondary operation of pulling the melted gallium to the edges of the PLA housing was required.

On the 3D printed samples, the coaxial cable was bent and pressed into the bent groove channel, although ease of assembly varied between samples printed on differing 3D printers. Zip ties held the cable tightly in place during the application of the radiator material, as well as for usage and handling of the completed antenna in a lab environment. Due to the low precisions of the 3D printed parts, the

conductive material could potentially flow into the cavity where the end of the cable rests, resulting in a short circuit between the center and outer conductors. Therefore, special care was required when applying conductive material near this area.

Out of the three conductive materials, the copper paint exhibited the best balance between performance and application, therefore, it was chosen as the conductive material for FBTA Rev 2, as shown in Figure 14.
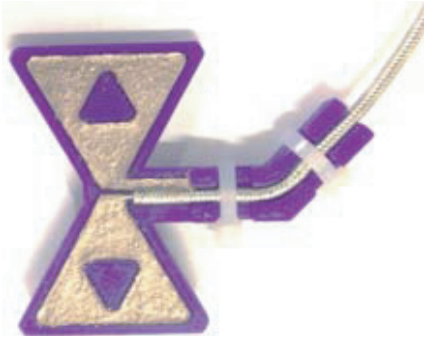
Figure 14. 3D printed FBTA Rev 2 sample with copper radiators.

Figure 15. Yagi-Uda antenna with copper radiators.

5.2. Yagi-Uda Antenna

The Yagi-Uda antenna is shown in Figure 15. Fabrication of Yagi-Uda antenna followed an identical process to the FBTA; however, the copper conductive paint was the only conductive material used to fill the negative space.

5.3. Spiral Antenna

After printing the spiral head structure, copper paint was applied to the radiators, as shown in Figure 16(a). The original cable termination design had pins on the PLA fixture standoffs and holes in the radiators; however, the 0.4 mm extruder diameter of the 3D printer was not able to produce the 1.2 mm ∅ holes on the 2.55 mm width of the radiators. Therefore, the pins were transferred to the radiators and the holes were placed in the fixture standoffs. A coaxial cable extends through the center hole with the inner conductor touching one radiator of the spiral and the outer conductor touching the protrusion from the other radiator. A zip tie was used to help secure the cable and create a better connection between the outer conductor and ground radiator. When printing the spiral design using conductive PLA, there were a few issues. During printing, the radiator pins and the ground radiator center protrusion melted due to the heat of the 3D printer extruder head. Therefore, the spiral had to be secured to the termination through super glue, and the carbon paint was used to improve the connection between the outer conductor and ground radiator. The resultant antenna is shown in Figure 16(b).

6. MEASUREMENT RESULTS

6.1. Fractal Bowtie Antennas

Two samples of each of FBTA Rev 1 were fabricated and tested. The S_{11} parameters were measured from 1 GHz to 4 GHz for both Rev 1 and Rev 2, with the measured results compared to the simulated results, shown in Figure 17. Figure 18 contains the S_{11} parameters of FBTA Rev 2, comparing the simulated results to the measured results of a sample with copper paint applied to the radiators. Although some
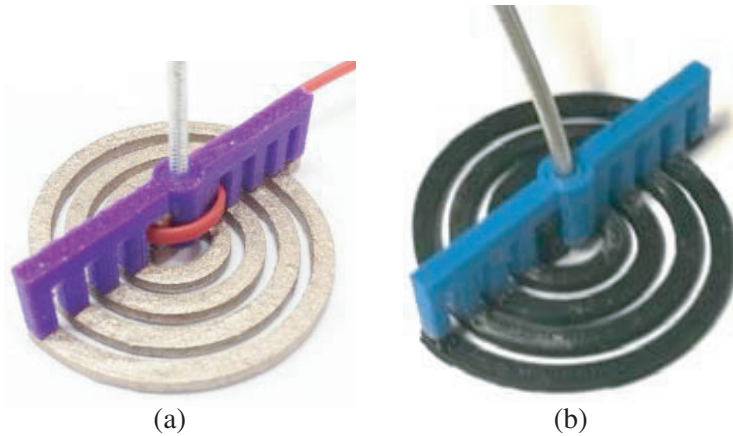
(a)   (b)

Figure 16. 3D printed PLA spiral antenna with (a) copper paint, and (b) conductive PLA radiators.
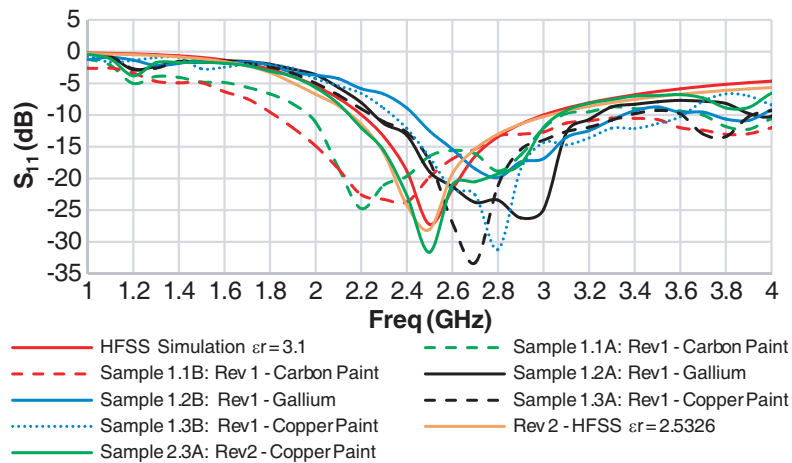

Figure 17. Reflection coefficient of varius FBTA antennas with varied radiator materials compared to simulation in resonant frequency range.
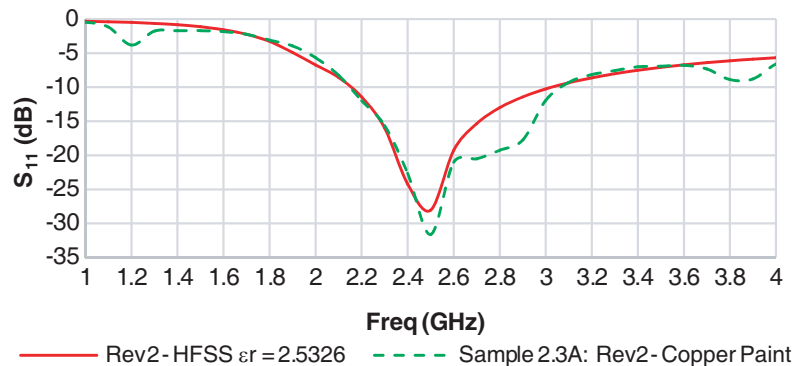

Figure 18. S_{11} of Rev 2 copper paint FBTA compared to simulation in resonant frequency range.

antennas performed better than others, all versions were matched at 2.45 GHz, within their -10 dB bandwidth. Additionally, the bandwidths of the antennas all exceeded the requirement of 500 MHz.

For FBTA Rev 1, a sample with copper paint was measured in the anechoic chamber. Figure 19 shows the co-polarization and cross-polarization of E-plane and H-plane, and Figure 20 shows the measured E-plane and H-plane compared to the simulation results.
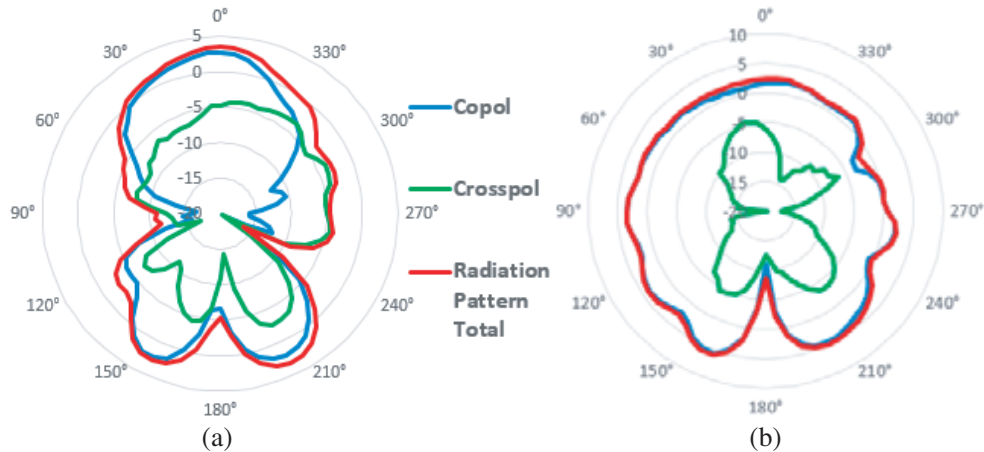
Figure 19. FBTA measured radiation pattern at 2.45 GHz in (a) E-plane and (b) H-plane.
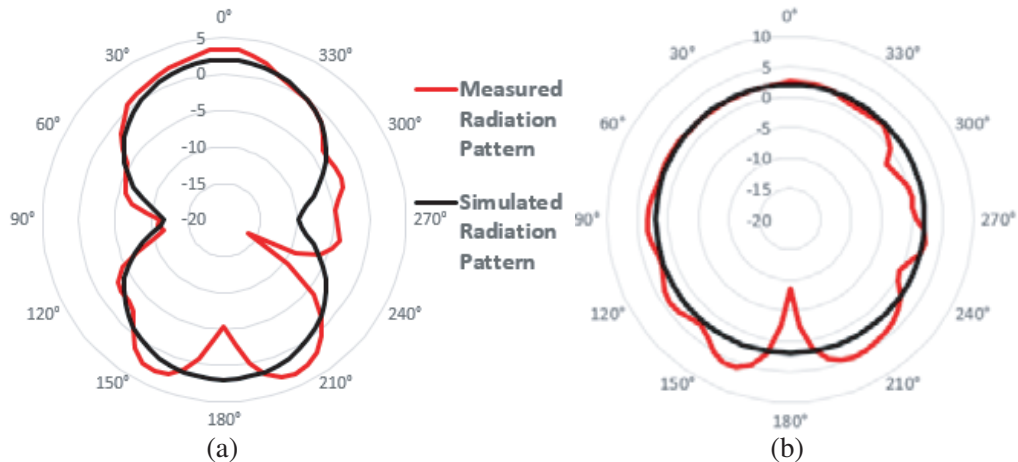
Figure 20. FBTA measured vs. simulated radiation pattern at 2.45 GHz in (a) E-plane and (b) H-plane.

6.2. Yagi-Uda Antenna

The Yagi-Uda antenna measured reflection coefficient and patterns are shown in Figures 21–23. The measured resonant frequency of the antenna is centered at 2.8 GHz, but 2.45 GHz is still within the -10 dB bandwidth of 700 MHz. One possible explanation for the extreme shift in the measured S_{11} is that the simulation model did not include the full cable termination geometry, but instead had a simplified termination. This could have caused a shift due to the extra substrate material added from manufacturing.

6.3. Spiral Antennas

Two samples for the spiral antenna were constructed: one using copper paint for the radiators and the other using conductive PLA. Figure 24 shows the results of reflection coefficient for the two samples compared with simulation. It is observed that the copper painted sample matched the simulations relatively well with a bandwidth of 10 GHz; however, the conductive PLA did not match at all. The conductive PLA is a very lossy conductor that is not suitable for antennas at the radio frequencies. For the radiation pattern measurement in the anechoic chamber, only the XZ-plane was measured due to the symmetry of the antenna. The measured radiation pattern compared to the simulated radiation pattern is shown in Figure 25.
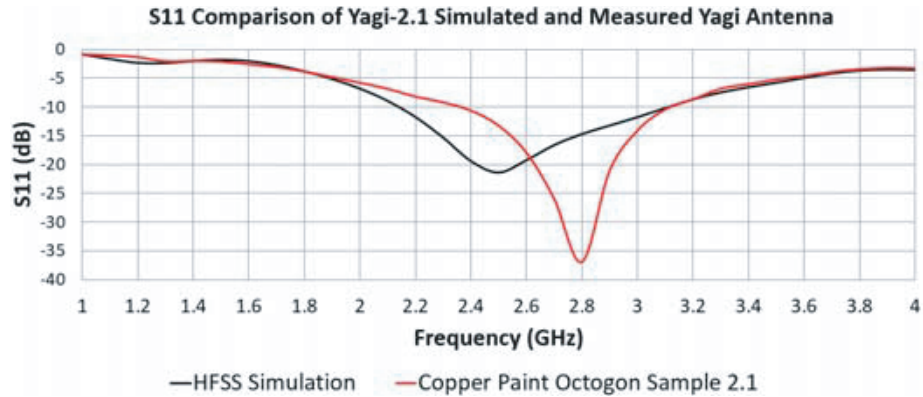
Figure 21. Simulated and measured reflection coefficient of Yagi-Uda antenna.
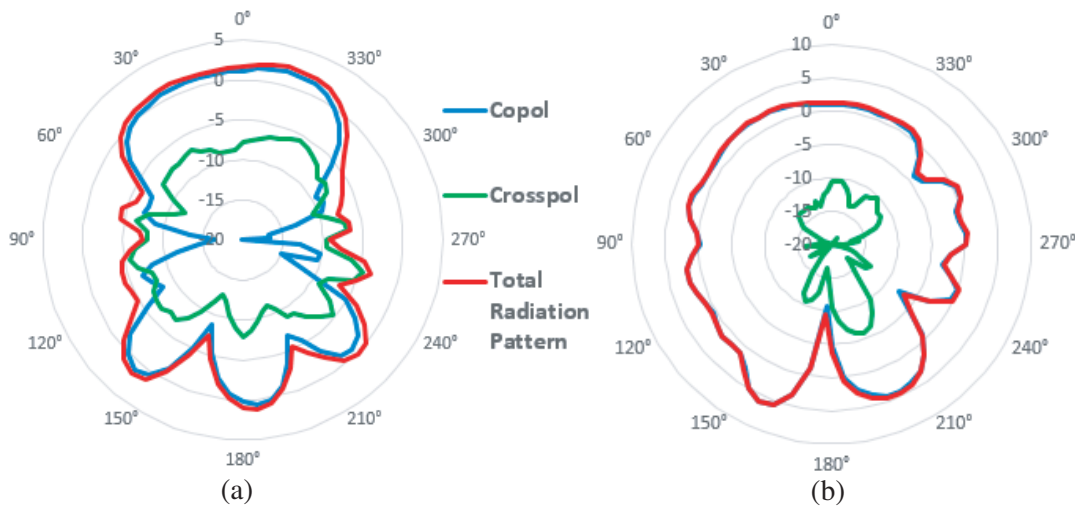

Figure 22. Measured radiation patterns at 2.45 GHz in (a) *E*-plane and (b) *H*-plane for Yagi-Uda antenna.
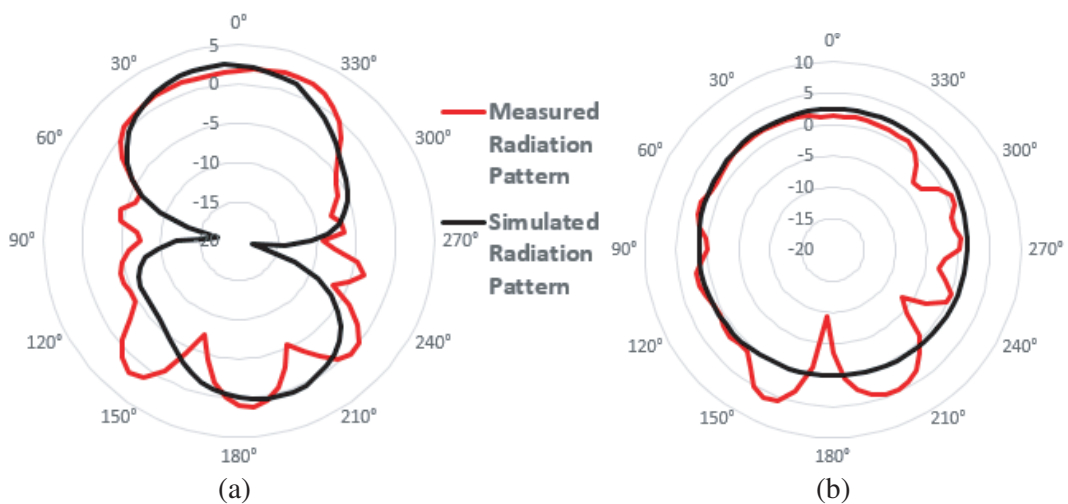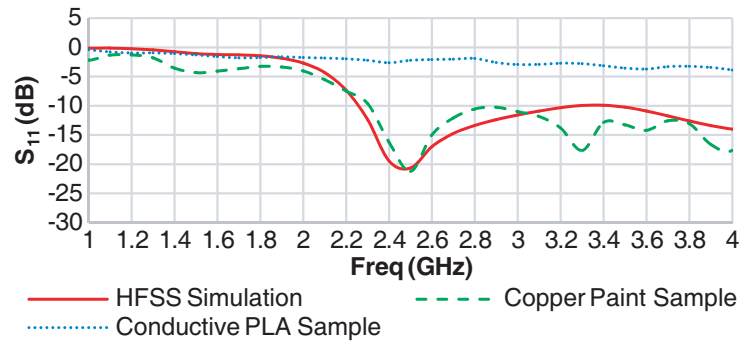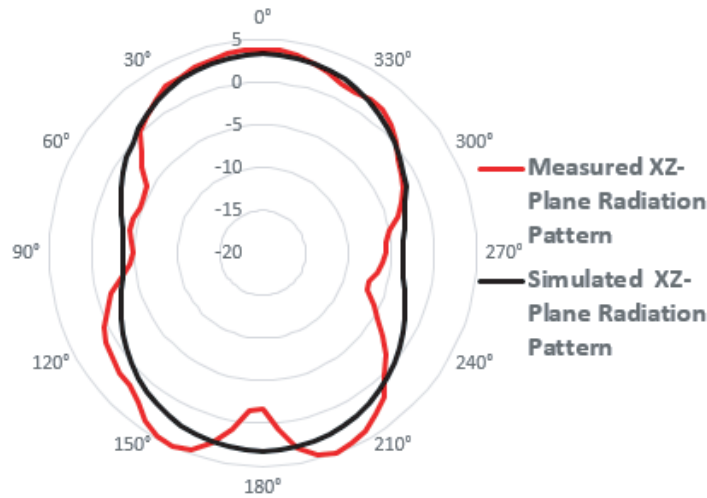

Figure 23. Measured vs. simulated radiation patterns at 2.45 GHz in (a) *E*-plane, and (b) *H*-plane for Yagi-Uda antenna.

Figure 24. S_{11} measured values of spiral antennas compared to simulation in resonant frequency range.

Figure 25. Spiral-2.1 measured vs. simulated radiation patterns at 2.45 GHz in XZ-plane.

7. CONCLUSION

This paper demonstrates the effort to fabricate three different antenna designs using 3D printing. First, material characterization using a coaxial transmission line apparatus was performed. The dielectric constants were determined for the dielectric and conductive PLA, which were of 2.53 and 9.35, respectively. Multiple antenna designs were simulated and optimized, and cable termination methods were proposed and applied to the completed designs. The 3D printed fractal bow-tie, Yagi-Uda, and spiral antennas utilizing the direct cable termination were found to have stable connections to the cable, with measured bandwidths of 540 to 1200 MHz, 400 to 500 MHz, and 2130 to 12200 MHz, respectively. The cable termination designs for these three antennas provided robust mechanical retention of the cable while providing good electrical performance through the elimination of mismatch reflections of additional connections to the cable feed. Overall, three unique Wi-Fi antennas were fabricated using 3D printing, with the final fabrication of all designs meeting the performance specifications of -10 dB bandwidth containing a 2.45 GHz resonant frequency.

REFERENCES

1. Nayeri, P., M. Liang, R. A. Sabory-Garcia, M. Tuo, F. Yang, M. Gehm, H. Xin, and A. Z. Elsherbeni, "3D printed dielectric reflectarrays: Low-cost high-gain antennas at sub-millimeter waves," *IEEE Trans. Antennas Propag.*, Vol. 62, No. 4, 2000–2008, Apr. 2014.

2. Floch, J.-M., B. El Jaafari, and A. El Sayed Ahmed, "New compact broadband GSM/UMTS/LTE antenna realized by 3D printing," *The 9th European Conference on Antennas and Propagation*, Lisbon, Portugal, Apr. 2015.

3. Lopez, A. G., E. L. C. Ernesto, R. Chandra, and A. J. Johansson, "Optimization and fabrication by 3D printing of a volcano smoke antenna for UWB applications," *7th European Conference on Antennas and Propagation (EuCAP)*, 1471–1473, Apr. 2013.

4. Mirzaee, M., S. Noghanian, and Y. Chang, "Low-profile bowtie antenna with 3D printed substrate," *Microw. Opt. Technol. Lett.*, Vol. 59, 706–710, 2017.

5. Ahmadloo, M. and P. Mousavi, "Application of novel integrated dielectric and conductive ink 3D printing technique for fabrication of conical spiral antennas," *IEEE Antennas and Propagation Society International Symposium (APSURSI)*, 780–781, Jul. 2013.

6. Mirzaee, M., S. Noghanian, L. Wiest, and Y. Chang, "Developing flexible 3D printed antenna using conductive ABS materials," *IEEE International Symposium on Antenna and Propagation and North American Radio Science Meeting 2015*, 1308–1309, Jul. 2015.

7. Ahn, B. Y., E. B. Duoss, M. J. Motala, X. Guo, S.-I. Park, Y. Xiong, J. Yoon, R. G. Nuzzo, J. A. Rogers, and J. A. Lewis, "Omnidirectional printing of flexible, stretchable, and spanning silver microelectrodes," *Science*, Vol. 323, No. 5921, 1590–1593, Mar. 2009.

8. Adams, J. J., S. C. Slimmer, J. A. Lewis, and J. T. Bernhard, "3D-printed spherical dipole antenna integrated on small RF node," *Electron. Lett.*, Vol. 51, No. 9, 661–662, Apr. 2015.

9. "Antenna fabrication via direct print," [online], available: http://www.sciperio.com/antenna/-antenna-fabrication.asp, Nov. 2017.

10. Bisognin, A., D. Titz, C. Luxey, G. Jacquemod, F. Ferrero, D. Lugara, A. Bisognin, R. Pilard, F. Gianesello, D. Gloria, J. R. Costa, C. Laporte, H. Ezzeddine, E. B. Lima, and C. A. Fernandes, "A 120 GHz 3D-printed plastic elliptical lens antenna with an IPD patch antenna source," *IEEE International Conference on Ultra-Wide Band (ICUWB)*, 171–174, Sep. 2014.

11. Yi, H., S.-W. Qu, K. B. Ng, and C. H. Chan, "3-D printed discrete dielectric lens antenna with matching layer," *International Symposium on Antennas and Propagation (ISAP)*, 115–116, Dec. 2014.

12. Bisognin, A., D. Titz, F. Ferrero, R. Pilard, C. A. Fernandes, J. R. Costa, C. Corre, P. Calascibetta, J.-M. Riviere, A. Poulain, C. Badard, F. Gianesello, C. Luxey, P. Busson, D. Gloria, and D. Belot, "3D printed plastic 60 GHz lens: Enabling innovative millimeter wave antenna solution and system," *IEEE MTT-S International Microwave Symposium (IMS)*, 1–4, Jun. 2014.

13. Garlotta, D., "A literature review of Poly (Lactic Acid)," *Journal of Polymers and the Environment*, Vol. 9, No. 2, 63–84, Apr. 2001.

14. "Keysight technologies basics of measuring the dielectric properties of materials," [online], available at http://literature.cdn.keysight.com/litweb/pdf/5989-2589EN.pdf, Nov. 2017.

15. Hoyack, M., J. Bjorgaard, E. Huber, M. Mirzaee, and S. Noghanian, "Connector design for 3D printed antennas," *2016 IEEE International Symposium on Antennas and Propagation*, Fajardo, Puerto Rico, June.–Jul. 2016.

16. Neetu, S. B. and R. K. Bansal, "Design and analysis of fractal antennas based on Koch and Sierpinski fractal geometries," *International Journal of Advanced Research in Electrical, Electronics and Instrumentation Engineering*, Vol. 2, No. 6, 1–7, Jun. 2013.

17. Amin, Y., Q. Chen, L. R. Zheng, and H. Tenhunen, "Design and fabrication of wideband Archimedean spiral antenna based ultra-low cost "green" modules for RFID sensing and wireless applications," *Progress In Electromagnetics Research*, Vol. 130, 241–256, 2012.

18. Liu, Q., C.-L. Ruan, L. Peng, and W.-X. Wu, "A novel compact Archimedean spiral antenna with gap-loading," *Progress In Electromagnetics Research Letters*, Vol. 3, 169–177, 2008.

19. Pozar, D. M., "Field analysis of transmission lines," *Microwave Engineering*, 1st Edition, Ch. 3, sec. 2–9, 72–107, Addison-Wesley, 1990.

20. Huber, E., M. Mirzaee, J. Bjorgaard, M. Hoyack, S. Noghanian, and I. Chang, "Dielectric property measurement of PLA," *2016 International Conference on Electro/Information Technology*, Grand

Forks, ND, USA, May 2016.

21. Ansys, [online], available at http://www.ansys.com/Products/Simulation+ Technology/-Electronics/Signal+ Integrity/ANSYS+ HFSS, Nov. 2017.

22. CST Microwave Studio, [online], available at https://www.cst.com/Products/CSTMWS, Nov. 2017.

23. Nakatsuka, T., "Polyactic acid-coated cable," *Fukikura Technical Review*, No. 40, 2011.

24. Bare Conductive Electric Paint, [online], available at https://www.bareconductive.com/shop/electric-paint-10ml/, Nov. 2017.

25. Caswell Copper Conductive Paint, [online], available at http://www.caswellplating.com/copper-conductive-paint-4oz.html#, Nov. 2017.

26. Galium by RotoMetal, https://rotometals.com/gallium/, Nov. 2017.